



Microstructure development during rapid alloy solidification

Kaihua Ji, Amy J. Clarke, Joseph T. McKeown, and Alain Karma*

Solidification processing of structural alloys can take place over an extremely wide range of solid–liquid interface velocities spanning six orders of magnitude, from the low-velocity constitutional supercooling limit of microns/s to the high-velocity absolute stability limit of m/s. In between these two limits, the solid–liquid interface is morphologically unstable and typically forms cellular-dendritic microstructures, but also other microstructures that remain elusive. Rapid developments in additive manufacturing have renewed the interest in modeling the high-velocity range, where approximate analytical theories provide limited predictions. In this article, we discuss recent advances in phase-field modeling of rapid solidification of metallic alloys, including a brief description of state-of-the-art experiments used for model validation. We describe how phase-field models can cope with the dual challenge of carrying out simulations on experimentally relevant length- and time scales and incorporating nonequilibrium effects at the solid–liquid interface that become dominant at rapid rates. We present selected results, illustrating how phase-field simulations have yielded unprecedented insights into high-velocity interface dynamics, shedding new light on both the absolute stability limit and the formation of banded microstructures that are a hallmark of rapid alloy solidification near this limit. We also discuss state-of-the-art experiments used to validate those insights.

Introduction

The study of solidification microstructure formation and selection is crucial to engineering and to the processing of advanced new materials. In many processes ranging from conventional casting to welding to additive manufacturing, a melt of metallic elements is transformed to a polycrystalline state by the advance of a solidification front in a positive temperature gradient, for example, when cooler crystalline grains nucleating on the outer walls of a casting or at the bottom of a weld or powder-bed-fusion melt pool grow toward a hotter molten zone. Depending on the size of this zone, which can vary from meter-size castings to powder bed particles of tens of microns, the heat extraction rate can increase by several orders of magnitude resulting in temperature gradients G in the range of $1\text{--}10^6$ K/m and solidification velocities V spanning $\mu\text{m/s}$ in conventional to m/s or higher in rapid solidification processes.

As illustrated in **Figure 1a**, the solid–liquid interface is morphologically unstable¹ over a large portion of the (V, G) plane, where cellular/dendritic microstructures are formed.

Those microstructures give rise to spatially inhomogeneous distributions of atomic elements in the final solidified material that impact mechanical and other properties. For low velocity, morphological instability is controlled by the competition between the destabilizing effect of the solute diffusion field ahead of the solid–liquid interface and the restabilizing effect of the temperature gradient. Above a critical velocity, V_{cs} , the solutal diffusion boundary layer ahead of the interface becomes sufficiently steep for a zone of liquid to become supercooled, thereby causing a perturbation of the interface to grow into the supercooled liquid. This constitutional supercooling criterion predicts that V_{cs} increases linearly with G as shown in **Figure 1a**,^{2,3} with $V_{cs} \sim \mu\text{m/s}$ for the low G range of conventional solidification. In contrast, for high velocity, instability is controlled by the competition between the destabilizing effect of the diffusion field and the restabilizing effect of capillarity, which reflects the tendency of the solid–liquid interface to remain flat to minimize its total excess free-energy. As a result, the maximum velocity beyond which a planar

Kaihua Ji, Physics Department and Center for Interdisciplinary Research on Complex Systems, Northeastern University, Boston, USA; Materials Science Division, Lawrence Livermore National Laboratory, Livermore, USA; jk5@llnl.gov

Amy J. Clarke, Department of Metallurgical and Materials Engineering, Colorado School of Mines, Golden, USA; Sigma Manufacturing Sciences Division, Los Alamos National Laboratory, Los Alamos, USA; amyclarke@mines.edu; aclarke@lanl.gov

Joseph T. McKeown, Materials Science Division, Lawrence Livermore National Laboratory, Livermore, USA; mckeown3@llnl.gov

Alain Karma, Physics Department and Center for Interdisciplinary Research on Complex Systems, Northeastern University, Boston, USA; a.karma@northeastern.edu

*Corresponding author

doi:10.1557/s43577-024-00717-6

solidification front is morphologically stable, known as the absolute stability limit and denoted by V_a , is independent of G , and of the order of m/s.

The past three decades have witnessed major progress in modeling cellular and dendritic microstructures that form over the wide range of velocity comprised between constitutional supercooling and absolute stability ($V_{cs} < V < V_a$), corresponding to the blue and orange shaded regions in Figure 1a, respectively. Much of this progress has been achieved by phase-field (PF) modeling,^{4–8} which circumvents front tracking by making the solid–liquid interface spatially diffuse. To date, however, PF formulations to quantitatively simulate alloy solidification have been primarily developed and validated for a low-to-intermediate V regime above constitutional supercooling where the solid–liquid interface can be assumed to remain in local thermodynamic equilibrium,^{9–13} or where the departure from equilibrium remains small enough to be treated as a perturbation.¹⁴ Most attempts to extend quantitative PF modeling to the far-from-equilibrium, high- V regime near absolute stability have been limited to one dimension (1D).^{15–19} As a result, microstructure formation in this high- V regime still remains poorly understood despite its practical relevance. In addition to the known advantages of additive manufacturing, rapid alloy solidification can produce new materials having superior properties to those processed at low solidification rates through extended solid solubility and by reducing or eliminating intercellular/dendritic microsegregation, leading to more homogeneous microstructures.

In this article, we describe recent progress to model quantitatively this high- V regime by the PF method. We first briefly review classical sharp-interface theories of nonequilibrium effects at the solid–liquid interface and microstructure formation, emphasizing long-standing questions pertaining to banded microstructures (Figure 1a), which are the hallmark of rapid alloy solidification beyond absolute stability.^{20–29} We then describe a recently developed, quantitative PF model for far-from-equilibrium alloy solidification that has reproduced for the first time banded microstructures and yielded unprecedented new insights into their formation.³⁰ We conclude by a quantitative comparison of PF simulations and state-of-the-art experiments that visualize *in situ* the solid–liquid interface,²⁹ thereby making it uniquely possible to validate some of these insights.

Sharp-interface models

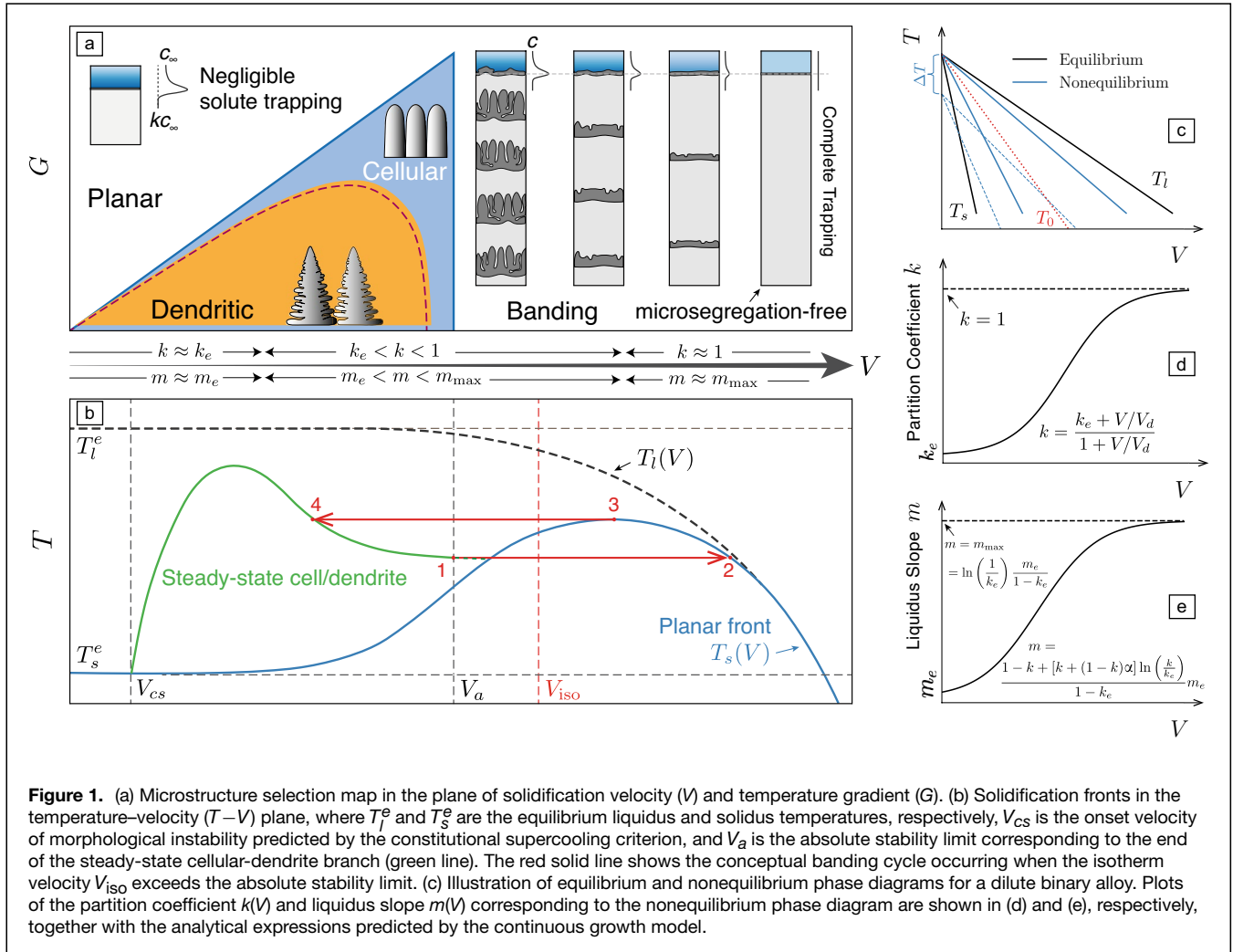
The conceptual framework to understand the formation of cellular/dendritic and banded microstructures over the entire V range is shown schematically in Figure 1b for a dilute binary alloy. This framework is derived from classical sharp-interface theories that treat the solid–liquid interface as a sharp boundary^{31,32} and incorporate nonequilibrium effects at the solid–liquid interface that become important at high velocities.^{33–35} Solidification generally takes place within the freezing range comprised between the equilibrium liquidus $T_l^e = T_M - m_e c_\infty$ and solidus $T_s^e = T_M - m_e c_\infty / k_e$ temperatures, where T_M is the elemental

material melting point, m_e and k_e are equilibrium values of the liquidus slope (defined here by its positive magnitude) and partition coefficient (ratio of the solidus and liquidus slopes), respectively, and c_∞ is the nominal alloy composition that fixes the solute concentration far ahead of the solidification front. As depicted in Figure 1c, nonequilibrium effects at the solid–liquid interface cause the alloy phase diagram to become velocity dependent. Two effects contribute to this departure. First, already in the absence of solute, a pure melt must solidify at a temperature $T < T_M$ at which the attachment rate of atoms at the interface from liquid to solid exceeds the detachment rate from solid to liquid. For metallic systems with an atomically rough solid–liquid interface, the velocity is linearly proportional to the undercooling $\Delta T = T_M - T$, leading to the relation $V = \mu_k \Delta T$, where μ_k is the atomic attachment kinetic coefficient of the order of m/s/K.^{6,36,37} Second, chemical equilibrium at the interface requires that the time $\sim W_0^2/D_l$ for solute to diffuse across the spatially diffuse solid–liquid interface, where W_0 is the interface thickness and D_l is the solute diffusivity in the liquid, be much shorter than the time to solidify this region $\sim W_0/V$. When these two times become comparable, which occurs when $V \sim V_d$, where $V_d \equiv D_l/W_0$ is the diffusive speed, incomplete partitioning causes solute to be trapped by the advancing interface. As a result of solute trapping, the concentrations on the solid and liquid sides of the interface, denoted by c_s and c_l , respectively, become closer. In sharp-interface models, where the solute concentration has a finite jump ($c_l - c_s$) at the interface, solute trapping has been modeled using a continuous growth (CG) model.^{34,35,38} This model yields velocity-dependent forms of the partition coefficient $k(V)$ and liquidus slope $m(V)$ shown schematically in Figure 1d–e, respectively. The form of $m(V)$ is affected by solute drag, which describes how part of the available solidification driving force is dissipated to redistribute solute and solvent atoms across the interface.³⁸ The velocity-dependent liquidus and solidus at some intermediate velocity $V \sim V_d$ are depicted by the blue lines in Figure 1c. They collapse at very high $V \gg V_d$ onto the T_0 line (red line in Figure 1c), which corresponds to the temperature at which the solid and liquid phases have equal chemical free-energies, and hence solidification can occur without partitioning (in the $k \rightarrow 1$ limit). The T_0 line has been drawn for clarity in Figure 1c by neglecting the kinetic undercooling ΔT . However, the actual liquidus and solidus presenting the complete velocity-dependent dilute alloy phase diagram, including ΔT , correspond to the blue dashed lines in Figure 1c.

Sharp-interface theories that incorporate those nonequilibrium effects provide analytical predictions for the absolute stability limit³¹

$$V_a = \frac{D_l m(V_a) c_\infty [1 - k(V_a)]}{k(V_a)^2 \gamma}, \quad 1$$

where $\gamma = \gamma_{sl} T_M / L$ is the Gibbs–Thomson coefficient, γ_{sl} is the excess free-energy of the solid–liquid interface, and L is



the latent heat of melting. They also predict the tip temperature of cellular/dendritic array structures,³² which is represented schematically by the green solid line in Figure 1b. The tip temperature first increases with $T \approx T_l^e - GD_l/V$ as cellular structures are formed above constitutional supercooling, and then decreases in a dendritic regime when the tip shapes become parabolic. For comparison, the temperature of a planar interface, which is morphologically unstable for $V_{cs} < V < V_a$, is given by the velocity-dependent liquidus with $c_l = c_\infty/k(V)$ imposed by mass conservation (i.e., the concentration far ahead in the liquid must be the same as in the solid in a steady state), yielding

$$T(V) = T_M - \frac{m(V)}{k(V)} c_\infty - \frac{V}{\mu_k}, \quad 2$$

which corresponds to the blue solid line in Figure 1b. The planar front temperature is seen to first increase due to solute trapping when $V \sim V_d$, corresponding to the second term on the right-hand side of Equation 2, and then decrease at higher velocity due to the kinetic undercooling, corresponding to the second term on the right-hand side of Equation 2.

Banded microstructures composed of alternating light and dark bands lying roughly parallel to the solidification front, which are depicted schematically in Figure 1a, have been observed in a wide range of alloys such as Ag-Cu,²⁰ Al-Cu,^{21,24,25,29,39} and Al-Fe.^{22,26} The observation of banded microstructures beyond absolute stability may seem contradictory, since a planar front is expected to be stable when the isotherm velocity exceeds V_a . However, absolute morphological stability only implies stability with respect to sinusoidal perturbations of the interface on the short submicron wavelengths of high- V cellular/dendritic microstructures, but not against perturbations of very large wavelength that can cause the interface velocity to transiently exceed or be less than the isotherm velocity imposed by the heat extraction rate. When the slope of the planar front temperature-velocity curve (blue solid line in Figure 1b) is positive, $dT(V)/dV > 0$, plane front growth is theoretically predicted to undergo an oscillatory instability at an infinite wavelength,⁴⁰ or a very long wavelength much larger than the primary spacing of cellular/dendritic microstructures when latent heat diffusion is taken into account.⁴¹

This instability is driven by solute trapping: as the interface accelerates, it traps more solute thereby accelerating further, since $k(V)$ is a monotonically increasing function of V . Based on this picture, banding has been hypothesized to consist of the limit cycle 1-2-3-4-1-2-3-4-1...depicted schematically in Figure 1b.²⁷ This cycle assumes that the interface quasi-instantaneously accelerates isothermally from the end of the steady-state dendrite branch (point 1 in Figure 1b) to the stable portion $dT(V)/dV < 0$ of the planar front temperature–velocity curve (point 2), remains planar from 2 to 3, slowly decelerating to form a light microsegregation-free band, then quasi-instantaneously decelerates isothermally to reform a dendritic array structure from 3 to 4, and finally slowly accelerates from 4 to 1 along the steady-state dendrite branch to form a dark band with a microsegregation pattern, at which point the cycle repeats.

To what extent this hypothesized banding cycle is representative of the actual interface dynamics has remained largely unknown. A theory based on this cycle predicts a band spacing that is inversely proportional to G and much larger than the observed spacing when reasonable estimates of G in laser remelting experiments are used as input into the theory.²⁷ A sharp-interface 1D numerical study by boundary integral method of plane front oscillations has demonstrated that the abrupt acceleration from 1 to 2 cannot occur isothermally when latent heat rejection at the interface is taken into account,^{41,42} but this study falls short of describing nonplanar structures within dark bands. As a result, basic microstructural pattern formation questions have remained unanswered. Does **Equation 1** accurately predict the absolute stability limit beyond which steady-state growth of dendritic array structures ceases to exist? How do these structures lose stability to initiate banding and what interface dynamics underlies the complete banding cycle? What controls the banding spacing? Over what range of composition does banding occur?

PF modeling and scale-bridging challenge

PF models of binary alloy solidification were introduced over three decades ago⁴³ following the introduction of the PF method for the solidification of pure melts.⁴⁴ However, despite the rapid growth in computing power, answering these questions has remained challenging. The main difficulty is that, in order to simulate microstructure development on experimentally relevant length- and time scales, the width of the spatially diffuse interface thickness in the PF model, referred to hereafter as W , needs to be chosen much larger than the microscopic width W_0 of the physical interface. The latter is of the order of 1 nm as measured by the spacial decay length of crystal density waves into the liquid, which occurs over several atomic layers in metallic systems with weak entropy of melting and atomically rough solid–liquid interfaces.⁴⁵ This computational constraint stems from the large disparity between W_0 and microstructural length scales such as the primary cellular/dendritic array spacing, which can vary from about a few hundred microns at low V near constitutional supercooling to

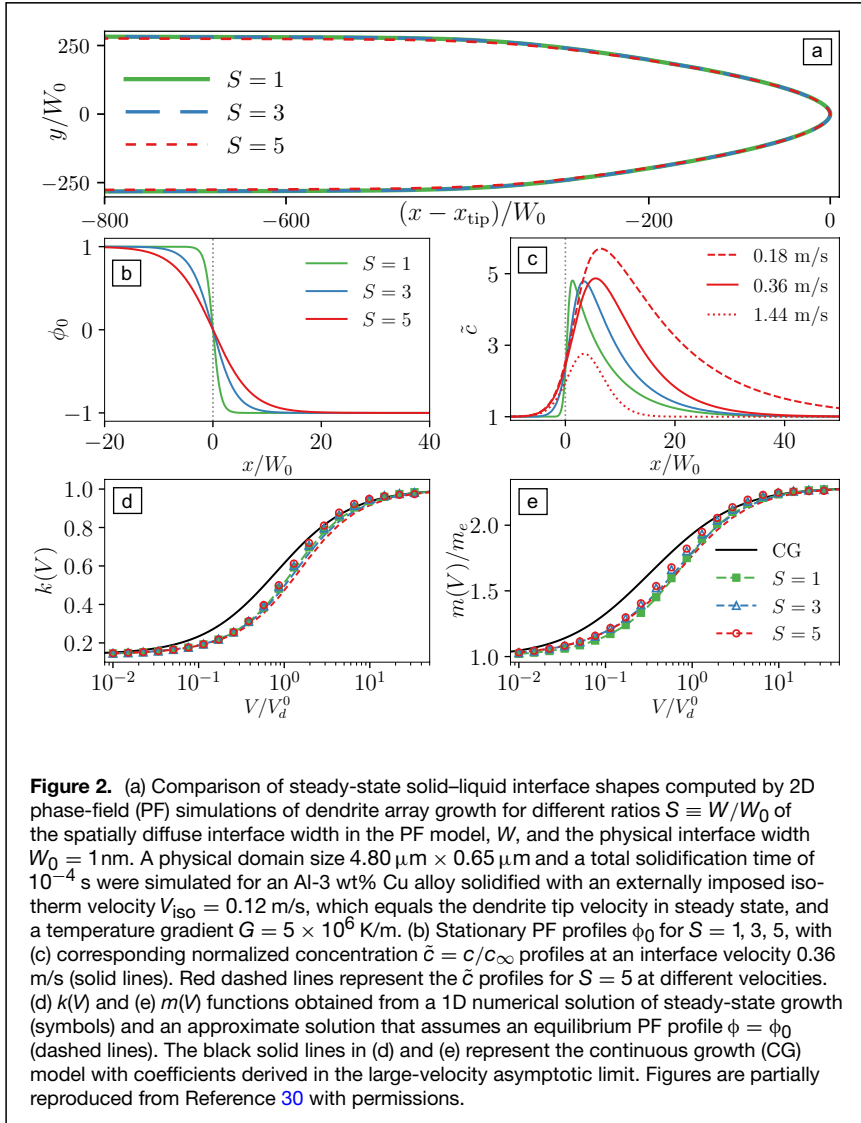
a few hundred nanometers at high- V near absolute stability. This disparity is smaller at high V , which makes it feasible to simulate in 2D a $\sim 3\text{-}\mu\text{m}^2$ physical domain size for 10^{-4} s with a realistic 1-nm interface width in ~ 30 h on a single Nvidia A100 GPU (**Table I**). This just suffices to simulate the steady-state growth of a single 2D dendrite in a spatially periodic dendritic array structure (**Figure 2a**), but not the growth of spatially extended microstructures on a much larger grain scale in 2D or 3D, which requires orders of magnitude larger computation times. The computational cost of PF simulations for a finite-difference implementation of the evolution equations on a regular grid with an explicit time stepping scheme scales approximately as $1/S^{2+d}$ where $S = W/W_0$ and d is the dimension of space; d in the exponent $2 + d$ reflects the reduction in the number of grid points when the interface thickness is increased and the additive factor of two stems from the numerical stability constraint on the time step.

How can this stringent computational limitation be overcome? To address this question, it is useful to write down the basic evolution equations for the phase field ϕ and the solute concentration field c

$$\frac{\partial \phi}{\partial t} = -K_\phi \frac{\delta F}{\delta \phi}, \quad 3$$

$$\frac{\partial c}{\partial t} = \vec{\nabla} \cdot \left(K_c(\phi, c) \vec{\nabla} \frac{\delta F}{\delta c} \right), \quad 4$$

which are traditionally derived variationally from a functional F representing the total free-energy of the system.⁴ Such a variational formulation guarantees that F decreases monotonically in time toward an equilibrium state. The interface width in the PF model is determined by the part of the free-energy density associated with the spatial variation of ϕ , which is the sum $\sigma |\vec{\nabla} \phi|^2/2 + f_{dw}(\phi)$ of a gradient square term and double-well potential $f_{dw}(\phi) = h(-\phi^2/2 + \phi^4/4)$, with minima of $f_{dw}(\phi)$ at $\phi = 1$ and $\phi = -1$ corresponding to the solid and liquid phases, respectively. Minimization of the total free-energy in 1D yields the classical equilibrium phase-field profile $\phi_0 = -\tanh(x/\sqrt{2}W)$ with $W = (\sigma/h)^{1/2}$ and the excess free-energy $\gamma_{sl} = (2\sqrt{2}/3)Wh$. As is well known, because γ_{sl} is proportional to the product of W and the barrier height h of the double-well potential, it is always possible to choose h for any W so as to reproduce the correct magnitude of γ_{sl} , which enters the Gibbs–Thomson condition determining the local equilibrium concentration of a curved interface. While W is a free parameter as far as capillarity is concerned, the same is not true for nonequilibrium effects at the interface. As reviewed in the previous section, solute trapping occurs when the interface velocity becomes comparable to the diffusive speed $V_d \sim D_l/W$. Because the PF model uses a spatially diffuse interface, it naturally captures solute trapping and solute drag. This was first shown over two decades ago in a 1D PF study of rapid alloy solidification, which demonstrated that **Equations 3** and **4** quantitatively reproduce the predictions



of the sharp-interface CG model for a subnanometer interface width.¹⁵ Unfortunately, this is no longer true when W is chosen much larger than W_0 ($S \gg 1$), causing V_d to be much smaller than its physical value and hence excess solute trapping when $V \sim V_d$. For the low- V regime, this difficulty has been circumvented by the introduction of an anti-trapping solute flux in

Table 1. Computation times in minutes for the 2D PF simulations of Figure 2a performed on a Nvidia A100 Graphics Processing Unit for different ratios $S \equiv W/W_0$ of PF and physical interface widths.

S	A	Simulation Time (min)
1	1	1894
3	6	25
5	12	4

Also listed are the values of the parameter A that are used to enhance the solute diffusivity within the spatially diffuse interface region so as to obtain the correct solute trapping properties shown in panels (d) and (e) of Figure 2 when $S > 1$.

Equation 4.⁹ This addition has been shown by an asymptotic thin-interface limit of the PF equations to counterbalance this excess trapping so as to restore local chemical equilibrium at the interface.^{9,10} This strategy has been widely used for quantitative PF modeling of solidification close to constitutional supercooling.^{5–8,46–49} It has also been shown to remain feasible when the departure from equilibrium is small.¹⁴ However, it has no obvious extension to model transient oscillatory phenomena like banding in a high- V regime, which requires quantitatively capturing solute trapping over a very large V range spanning cm/s to several m/s. Over this range, the partition coefficient $k(V)$ varies from a value close to its equilibrium value k_e to a value close to unity corresponding to complete trapping.

A recently developed alternative strategy to overcome the computational limitation associated with a large interface width is to enhance the solute diffusivity within the spatially diffuse interface region.³⁰ This strategy stems directly from the scaling of the diffusive speed, $V_d \sim D_l/W$, which implies that the correct physical magnitude of V_d can be reproduced even when $W \gg W_0$ as long as D_l is chosen much larger than its physical value within the spatially diffuse interface region, where

ϕ is spatially varying. This is possible because the diffusivity within this region varies with ϕ in the PF model. In the dilute limit of alloy solidification considered here, it is controlled by the function $q(\phi)$ that determines $K_c(\phi, c) = v_0 D_l q(\phi) c / (RT_M)$ in Equation 4, where v_0 is the molar volume and R the gas constant. Thus, it is possible to choose $q(\phi)$ so as to enhance solute diffusion inside the interface region, while keeping its value in the liquid phase away from the interface unchanged. A simple choice that fulfills this requirement is $q(\phi) = A(1 - \phi)/2 - (A - 1)(1 - \phi)^2/4$. This form interpolates linearly between D_l in the liquid ($\phi = -1$) and approximately 0 in the solid ($\phi = 1$) when $A = 1$, which is the commonly used form that neglects diffusion in the solid state. However, for $A > 2$, $q(\phi)$ has a maximum value $A^2/[4(A - 1)]$ at $\phi = -1/(A - 1)$ that enhances solute diffusivity to compensate excess trapping. This strategy is analogous to the one previously mentioned used to model capillarity, which involves lowering h to compensate for a large W so that $\gamma_{sl} \sim Wh$

retains its physical value. Here, D_l is increased in the interface region to keep V_d essentially constant when W is increased. The implementation of this strategy is somewhat more complicated because solute trapping properties are characterized by velocity-dependent functions $k(V)$ and $m(V)$, in contrast to a single materials parameter like γ_{sl} , which are in turn controlled by the choice of the function $q(\phi)$ in the PF model. However, the above form of $q(\phi)$ suffices to reproduce desired $k(V)$ and $m(V)$ functions over the entire V range for different choices of interface width. This is illustrated in Figure 2b–c, which compares the 1D phase field and corresponding concentration profiles for a moving planar interface for three different interface widths corresponding to $S = 1$, the reference case for a physical interface width of 1 nm, and $S = 3$ and $S = 5$ corresponding to a 3 and 5 times larger width, respectively. The values $A = 1, 6, \text{ and } 12$ were used for $S = 1, 3, \text{ and } 5$, respectively. The concentration profiles have different shapes but, importantly, they all have the same peak value of the concentration at the same velocity. Hence, they yield the same value of the partition coefficient $k(V) = c_s/c_l$, and can also be shown to yield the same value of $m(V)$.³⁰ This remains true over a large range of velocity as shown in Figure 2d–e, which compares computed values of $k(V)$ and $m(V)$, respectively, for three values of S . The comparison of steady-state interface shapes in Figure 2a shows that the same microstructures can be obtained with a much larger interface width with a computation time reduced by three orders of magnitude (Table I), thereby making it possible to address for the first time the

long-standing questions of microstructural pattern formation raised at the end of the second section.

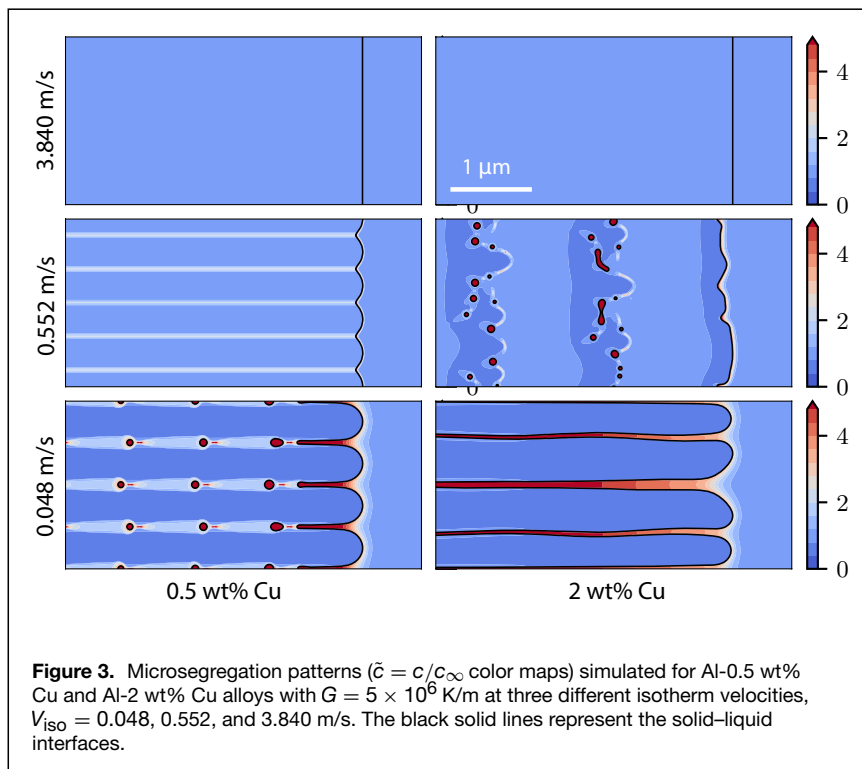
New insights into microstructure development far-from-equilibrium

To address these questions, we model the rapid directional solidification of dilute Al-Cu alloys in 2D using anisotropic forms of the excess interface free-energy $\gamma_{sl}(\theta) = \gamma_{sl}^0[1 + \epsilon_s \cos(4\theta)]$, and kinetic coefficient $\mu_k(\theta) = \mu_k^0[1 + \epsilon_k \cos(4\theta)]$ with fourfold cubic symmetry. Here, θ is the angle between the direction normal to the interface and the x -axis, corresponding to the growth of a single crystal with one of the $[100]$ crystal axes aligned parallel to the growth direction that coincides with the x -axis. Because most of the sharp-interface theories reviewed in the second section neglect latent heat rejection, we first use the standard frozen temperature approximation that assumes a linear temperature gradient $T = T_M + G(x - V_{\text{iso}}t)$ along the growth direction and a fixed isotherm velocity V_{iso} , which fixes the solidification rate. For computational efficiency, all simulations are carried out with $S = 5$ that yields converged interface shapes (Figure 2a) with dramatically reduced computation time (Table I). Simulations are started with a planar interface at rest at the liquidus temperature. All the materials parameters and details of the simulations can be found in Reference 30.

Simulated microstructures for two different compositions and increasing isotherm velocity V_{iso} in the range of absolute stability are shown in Figure 3. They reveal that, below a critical composition comprised between 0.5 and 2 wt% Cu, absolute stability is reached with increasing V_{iso} by a smooth transition from deep cells to shallow cells to a planar interface.

For 0.5 wt% Cu, this transition occurs at a velocity between 0.5 and 0.6 m/s, which is about twice the value predicted by Equation 1, $V_a \approx 0.32$ m/s. In contrast, for larger composition (e.g., 2 wt% Cu in Figure 3), the transition is abrupt. Below a critical isotherm velocity, $V_{\text{iso}} < V_c^1$, a deep cellular/dendritic array structure is formed. For $V_{\text{iso}} > V_c^1$, an initially planar interface evolves directly into an oscillatory cycle producing banded microstructures. Banding persists over a wide range of V_{iso} , followed by restabilization to a planar morphology at much larger V_{iso} close to the maximum of the temperature–velocity curve corresponding to point 3 in Figure 1b.

V_c^1 is significantly smaller than the absolute stability limit V_a predicted by Equation 1, for example, $V_c^1 \approx 0.45$ m/s versus $V_a \approx 0.86$ m/s



for 3 wt% Cu. Simulations also reveal that the onset velocity of banding depends on the initial condition. In traditional rapid solidification experiments, including laser track remelting^{20–27} and spot melting of thin films²⁹ discussed in the next section, V_{iso} increases progressively as the melt pool resolidifies and hence approaches the absolute stability limit with a cellular/dendritic microstructure already formed, as opposed to a planar interface initial condition. We simulated this scenario by slowly ramping up V_{iso} for a 3 wt% Cu alloy. In this case, the transition to banding occurs above a critical velocity $V_c^2 \approx 0.88$ m/s, which is close to the prediction of Equation 1, $V_a \approx 0.86$ m/s, and almost twice larger than $V_c^1 \approx 0.45$ m/s. For $V_c^1 < V_{\text{iso}} < V_c^2$, the interface dynamics is fundamentally bistable (i.e., two dynamical attractors consisting of a steady-state cellular/dendritic microstructure or a banded microstructure are attained depending on whether V_{iso} is ramped up or constant starting from a planar morphology, respectively).

Further insight into the origin of this bistability is provided by the simulation in **Figure 4**. The time sequence illustrates the interface dynamics for banded microstructure formation starting from a plane front initial condition at an isotherm velocity of 0.46 m/s just above V_c^1 . The results reveal that microsegregation-free solidification occurs by a rapid acceleration of the interface, which is initiated in the interdendritic tail region far behind the dendrite tips. Following this tail instability, the interface spreads rapidly laterally to suppress the growth of the dendritic front leading to planar front growth and forming a microsegregation-free band. The planar front then decelerates and becomes again morphologically unstable to form a cellular/dendritic interface. In contrast, when V_{iso} is ramped up starting from a cellular/dendritic structure with deep narrow liquid grooves that suppress the tail instability, the instability leading to the formation of microsegregation-free bands is initiated at the dendrite tips at a higher isotherm velocity.³⁰ We conclude from those simulations that the onset velocity of banding depends sensitively on the location along the solid–liquid interface, where the rapid acceleration of the interface driven by solute trapping occurs first.

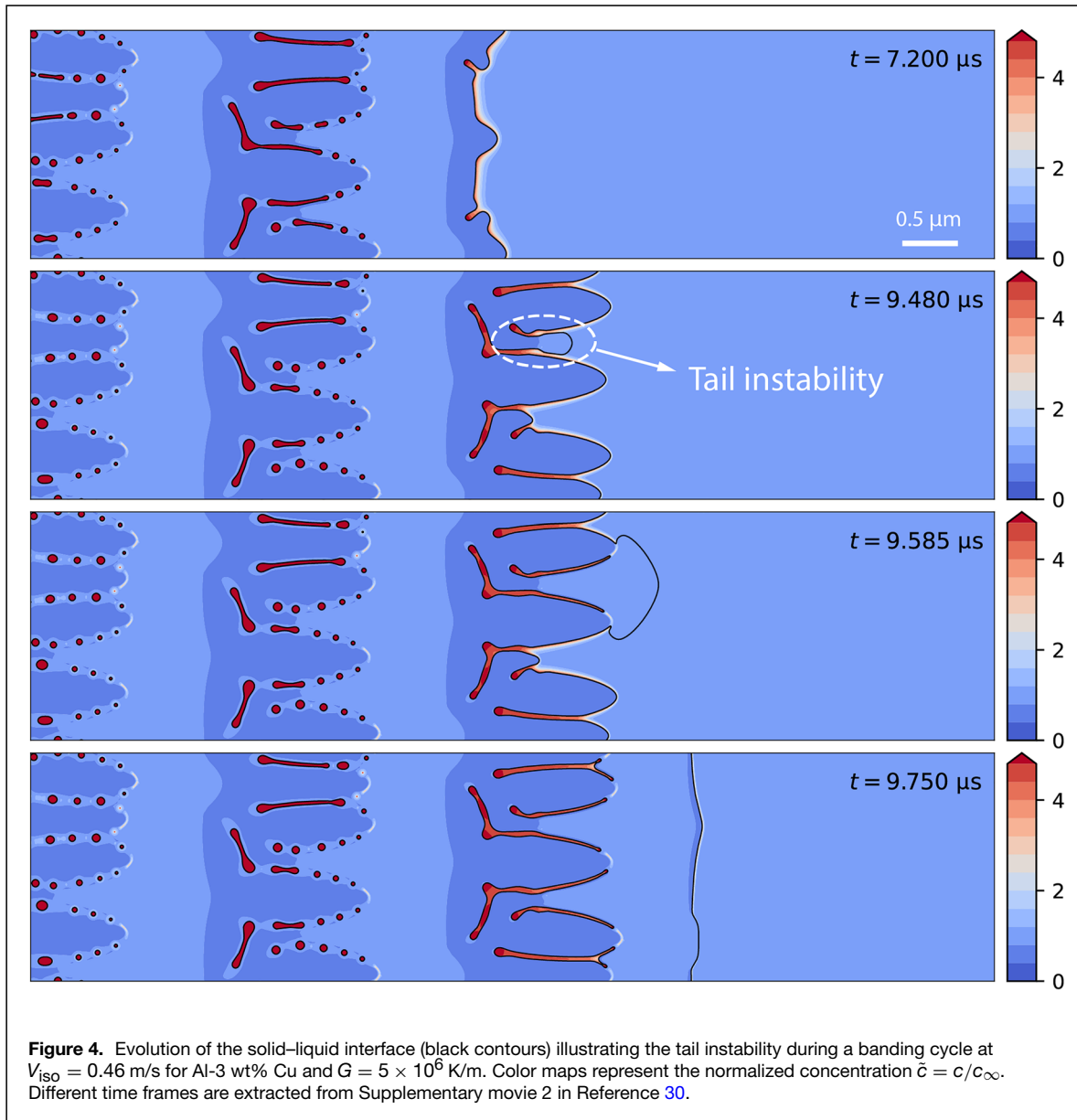
Next, we show in **Figure 5** banded microstructures for different isotherm velocities and the corresponding cycles in the temperature–velocity (T – V) plane. The instantaneous solidification front temperature is plotted versus the instantaneous front velocity that exhibits large variations around the isotherm velocity during banding. Superimposed on the T – V plane are the steady-state curves corresponding to stable dendritic array growth (red curve) for $V < V_c^2$ and planar front growth (blue curve) computed using Equation 2. The simulated banding cycle of **Figure 5a** for an isotherm velocity close to V_a follows reasonably well the conceptual banding cycle of **Figure 1b** discussed in the Introduction. At this velocity, microsegregated and microsegregation-free bands corresponding to the dendritic array and planar front growth, respectively, are of comparable width. In contrast, the cycles of **Figure 5b–c** make larger loops in the T – V plane when planar front growth occupies a larger fraction of the whole banding cycle, which is

no longer constrained to follow the 4-1 segment corresponding to steady-state dendritic array growth.

The most dramatic new insight concerns the role of latent heat rejection, which can be included by supplementing Equations 3 and 4 with an evolution equation for the temperature field.³⁰ The latent heat rejected by the moving solid–liquid interface produces a heat flux $\sim LV$ that can perturb the thermal field when it becomes comparable to the heat flux imposed by the externally imposed temperature gradient $\sim c_p D_T G$, where c_p is the specific heat at constant pressure and D_T is the thermal diffusivity (assumed here for simplicity to have equal values in the solid and liquid phases). For rapid solidification of metallic alloys under high G conditions, those two heat fluxes typically become of comparable magnitude when the interface velocity reaches the range of m/s (e.g., for the present simulation parameters $L/c_p = 340$ K, $D_T = 5.25 \times 10^{-5}$ m²/s, and $G = 5 \times 10^6$ K/m, $LV/(c_p D_T G) \approx 1.3$ for $V = 1$ m/s). Consequently, the frozen temperature approximation, which assumes a linear thermal profile is only valid for low velocities ($V \ll 1$ m/s) but not for the V range where banding occurs. In this range, large and rapid variations of interface velocity significantly alter the temperature profile in the interface region.^{41,42} The comparison of **Figure 5c–d** shows that latent heat rejection dramatically reduces the band spacing from several μm to a few hundred nm. **Figure 5d** further reveals that bands grow at a small angle with respect to the thermal axis due to the fact that the lateral spreading velocity of the interface that produces microsegregation-free bands is slowed down by latent heat rejection. As a result, the corresponding banding cycle in **Figure 5f** is shrunk considerably and makes a smaller loop in the T – V plane. The present PF model and the CG model both predict that $k(V)$ approaches a value close to unity during the high-velocity portion of the banding cycle ($V \gg V_d$), while both molecular dynamics simulations⁴⁵ and other theoretical models of solute trapping^{50,51} predict that complete trapping may occur (i.e., $k(V) = 1$) beyond some upper critical velocity about one order of magnitude larger than V_d . We do not expect this difference, i.e., whether $k(V)$ is close to or exactly unity, to have a significant impact on the conceptual banding cycles predicted by the frozen temperature approximation (FTA cycles in **Figure 5f**). More importantly, for the experimentally relevant banding cycle with the inclusion of latent heat (TFC cycle in **Figure 5f**), V remains in a range below complete trapping that we expect to be reasonably well described by the PF and CG models.

Quantitative comparison with experiments

Banded microstructures were first observed nearly four decades ago²⁰ and studied extensively during the 1990s by laser track remelting experiments.^{21–27} These experiments make it possible to characterize *post mortem* the microstructures by metallographic analysis and to infer the isotherm velocity, which increases from bottom to top of the melt pool to attain the laser track speed. The microstructure can then be correlated with V_{iso} at different locations of the melt pools. However, such



experiments do not make it possible to observe the dynamics of the solid–liquid interface underlying microstructure development. In this respect, the development of dynamic transmission electron microscopy (DTEM) has provided a major advance by enabling this *in situ* visualization during rapid resolidification of thin metallic films,^{29,52–55} as illustrated in **Figure 6**. These experiments use a short laser pulse to create an elliptical melt pool that then rapidly solidifies. DTEM is then used to image the growth of the solid–liquid interface at different instants of time, as shown in **Figure 6a–b** at different magnifications for an Al-9 wt% (Al-4 at.%) Cu alloy. This makes it possible to measure the elliptical solidification front velocity that increases with time as shown in **Figure 6c**; in addition, the microstructure

can be examined *post mortem* and correlated with the interface dynamics. At the larger velocity close to the center of the melt pool, cellular/dendritic array growth is seen to be terminated by the transition to a banded microstructure. As shown by the red arrow in **Figure 6b**, microsegregation-free bands spread laterally at a speed ≈ 6.6 m/s, which can be estimated by comparing the solidification front images at 32 and 32.5 μs . In addition, the measured band spacing extracted from **Figure 6c** is about 400 nm.

We carried out PF simulations for the same Al-9 wt% alloy, including latent heat rejection by increasing V_{iso} from 0.3 to 1.8 m/s over a time period of 30 μs based on the velocity measurements of **Figure 6c**. The simulated banded microstructure is

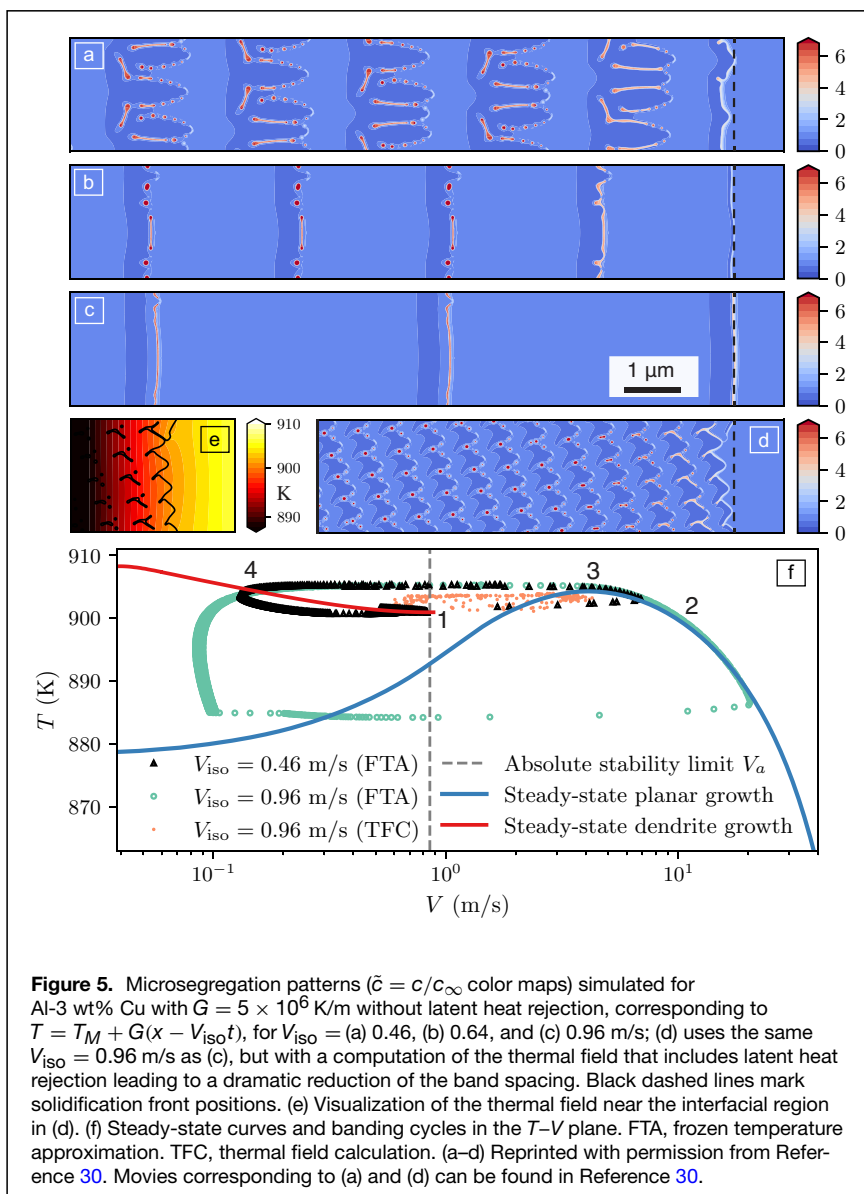


Figure 5. Microsegregation patterns ($\bar{c} = c/c_\infty$ color maps) simulated for Al-3 wt% Cu with $G = 5 \times 10^6$ K/m without latent heat rejection, corresponding to $T = T_M + G(x - V_{iso}t)$, for $V_{iso} =$ (a) 0.46, (b) 0.64, and (c) 0.96 m/s; (d) uses the same $V_{iso} = 0.96$ m/s as (c), but with a computation of the thermal field that includes latent heat rejection leading to a dramatic reduction of the band spacing. Black dashed lines mark solidification front positions. (e) Visualization of the thermal field near the interfacial region in (d). (f) Steady-state curves and banding cycles in the T - V plane. FTA, frozen temperature approximation. TFC, thermal field calculation. (a-d) Reprinted with permission from Reference 30. Movies corresponding to (a) and (d) can be found in Reference 30.

shown in Figure 6e. The band spacing is in excellent agreement with the experiments. Furthermore, the bands form by the same lateral spreading mechanism shown in Figure 5d with a lateral velocity of ≈ 6.7 m/s that closely matches the experimental value. This quantitative comparison brings direct unambiguous confirmation of the PF prediction that bands form by a lateral spreading mechanism, which differs markedly from the conceptual model of banding of Figure 1b, and indirect confirmation of the crucial role of latent heat rejection by the observation of a submicron band spacing that only matches the prediction of PF modeling with the inclusion of latent heat rejection. It is worth noting that the metallic films investigated experimentally have a finite thickness in the range of 50–150 nm. Hence, their geometry is inherently 3D while the present modeling is restricted

to 2D. However, under the assumption that the solid–liquid interface forms a meniscus of approximately constant curvature in the direction perpendicular to the film, we expect 2D simulations to provide a reasonable approximation of the growth dynamics in the plane of the film on a scale larger than the film thickness. The agreement between measured and predicted band spacings supports the validity of this quasi-2D modeling approximation. Capturing details of the microsegregation pattern in the interdendritic region would still require fully 3D simulations.

Conclusion

PF modeling has reached a mature stage where it is now possible to quantitatively simulate microstructure development during alloy solidification over an extremely wide range of growth rates, spanning near- to far-from-equilibrium conditions relevant for a wide range of conventional and rapid solidification processes, including additive manufacturing. As illustrated here, PF modeling has yielded unprecedented novel insights into banded microstructure formation and enabled the validation of these insights by quantitative comparison with state-of-the-art experiments. However, some challenges remain. Most of these insights have been obtained by 2D simulations that model, at least approximately, thin-film resolidification experiments.

Three-dimensional modeling, which is relevant for most applications, remains limited to small domain sizes that can at most resolve microstructures within a single grain. This may already suffice to make some practically useful predictions, such as determining alloy compositions and far-from-equilibrium processing conditions yielding improved microstructures with reduced or suppressed microsegregation. However, further scale bridging between PF modeling and other more coarse-grained methods remains needed to quantitatively model both the microstructure and grain structures at the scale of an entire 3D melt pool. There has been recent progress in this direction,^{56–59} but scale bridging under the far-from-equilibrium conditions discussed here remains largely unexplored.

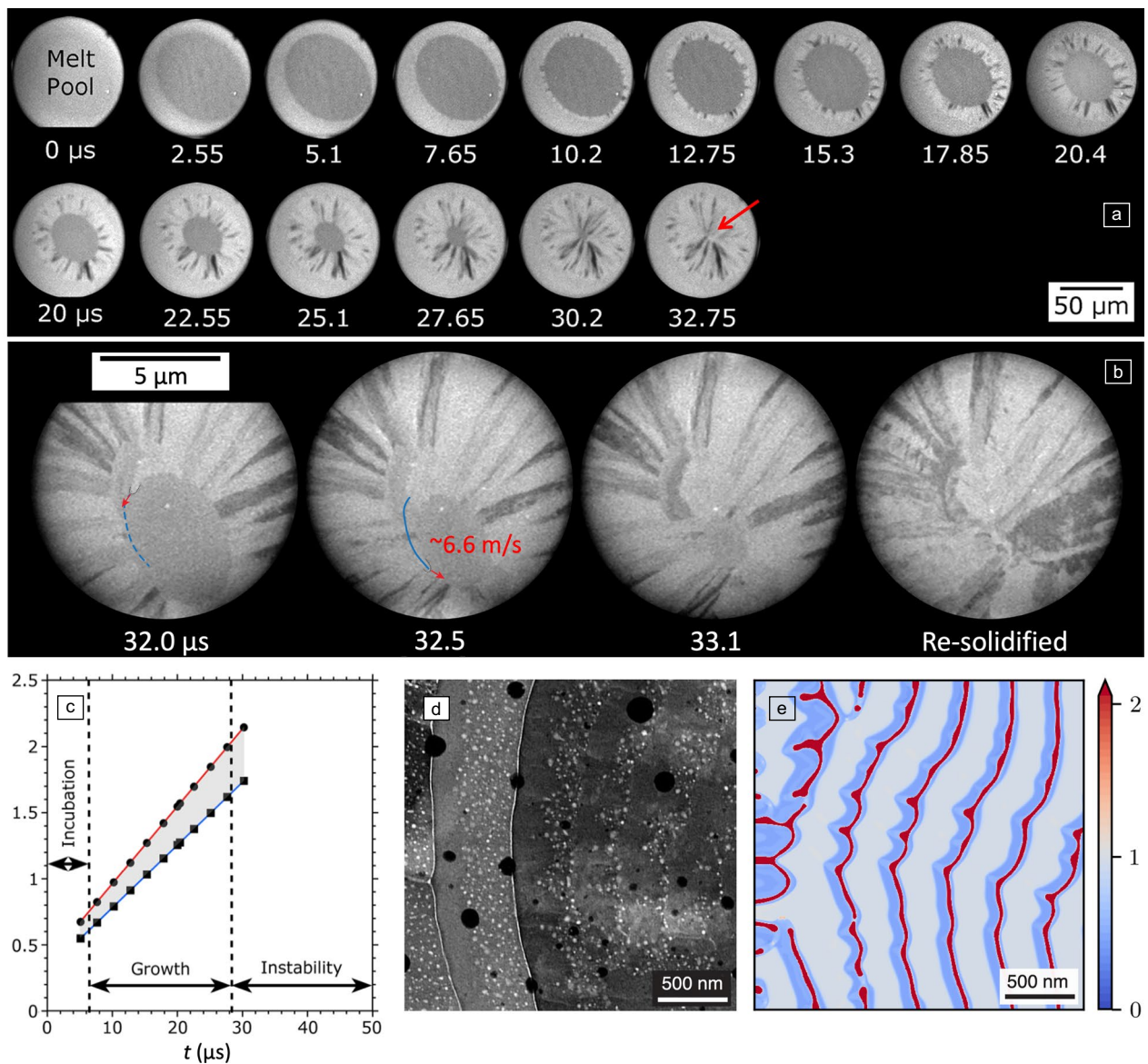


Figure 6. (a) Sequential time-delay images showing the evolution of the melt pool during rapid solidification in an Al-9 wt% Cu (Al-4 at.% Cu) alloy thin film after pulsed-laser melting. The times below each image represent the delays (in ms) between the peak of the Gaussian laser pulse that melted the film and the 50-ns electron pulse used to form the image. (b) Enlarged images illustrating the lateral growth leading to banded microstructures. Red arrows indicate the growth directions, while blue lines trace the trajectories of the laterally growing solidification front. (c) Time evolution of the velocity at the solidification front toward the center. The gray area indicates the velocity range across the solid-liquid interface. Velocities were measured along the semi-major and semi-minor axes of the elliptical melt pool, indicated, respectively, by the red and blue lines in the velocity plot. Comparison of banded microstructures from (d) a representative resolidified Al-9 wt% Cu alloy and (e) a 2D phase-field simulation ($\bar{c} = c/c_{\infty}$ color map) incorporating latent heat and $G = 5 \times 10^6$ K/m. The red arrow in (a) indicates the location where the detailed banded microstructure was examined after solidification. Reprinted with permission from References 29 and 30.

Acknowledgments

This work was supported by the US Department of Energy (DOE), Office of Science, Basic Energy Sciences (BES) under Award Nos. DE-SC0020895 and DE-SC0020870. Work at Lawrence Livermore National Laboratory was performed under the auspices of the US Department of Energy under Contract No. DE-AC52-07NA27344.

A.J.C. also acknowledges support by the US Department of Energy through the Los Alamos National Laboratory during the preparation of this manuscript. Los Alamos National Laboratory is operated by Triad National Security, LLC, for the National Nuclear Security Administration of US Department of Energy (Contract No. 89233218CNA000001).

Author contributions

A.K. wrote the manuscript and K.J. prepared all the figures. A.J.C. and J.T.M. provided input for the experimental section. K.J., A.J.C., and J.T.M. reviewed and edited the manuscript.

Funding

Open access funding provided by Northeastern University Library. US Department of Energy (DOE), Office of Science, Basic Energy Sciences Award Nos. DE-SC0020895 and DE-SC0020870. Lawrence Livermore National Laboratory under DOE Contract No. DE-AC52-07NA27344. Los Alamos National Laboratory under DOE Contract No. 89233218CNA000001.

Conflict of interest

The authors state that there are no conflicts of interest.

Open Access

This article is licensed under a Creative Commons Attribution 4.0 International License, which permits use, sharing, adaptation, distribution and reproduction in any medium or format, as long as you give appropriate credit to the original author(s) and the source, provide a link to the Creative Commons licence, and indicate if changes were made. The images or other third party material in this article are included in the article's Creative Commons licence, unless indicated otherwise in a credit line to the material. If material is not included in the article's Creative Commons licence and your intended use is not permitted by statutory regulation or exceeds the permitted use, you will need to obtain permission directly from the copyright holder. To view a copy of this licence, visit <http://creativecommons.org/licenses/by/4.0/>.

References

- W.W. Mullins, R.F. Sekerka, *J. Appl. Phys.* **35**(2), 444 (1964). <https://doi.org/10.1063/1.1713333>
- W. Kurz, D.J. Fisher, *Fundamentals of Solidification* (Trans Tech Publications, Zurich, 1989)
- J.A. Dantzig, M. Rappaz, *Solidification*, 2nd edn. (EPFL Press, Lausanne, 2016)
- W.J. Boettinger, J.A. Warren, C. Beckermann, A. Karma, *Annu. Rev. Mater. Res.* **32**, 163 (2002). <https://doi.org/10.1146/annurev.matsci.32.101901.155803>
- I. Steinbach, *Model. Simul. Mater. Sci. Eng.* **17**(7), 073001 (2009). <https://doi.org/10.1088/0965-0393/17/7/073001>
- A. Karma, D. Tourret, *Curr. Opin. Solid State Mater. Sci.* **20**(1), 25 (2016). <https://doi.org/10.1016/j.cossms.2015.09.001>
- W. Kurz, M. Rappaz, R. Trivedi, *Int. Mater. Rev.* **66**(1), 30 (2020). <https://doi.org/10.1080/09506608.2020.1757894>
- D. Tourret, H. Liu, J. Llorca, *Prog. Mater. Sci.* **123**, 100810 (2022). <https://doi.org/10.1016/j.pmatsci.2021.100810>
- A. Karma, *Phys. Rev. Lett.* **87**, 115701 (2001). <https://doi.org/10.1103/PhysRevLett.87.115701>
- B. Echebarria, R. Folch, A. Karma, M. Plapp, *Phys. Rev. E Stat. Phys. Plasmas Fluids. Relat. Interdiscip. Topics* **70**(6), 061604 (2004). <https://doi.org/10.1103/PhysRevE.70.061604>
- R. Folch, M. Plapp, *Phys. Rev. E Stat. Nonlin. Soft Matter Phys.* **72**(1), 011602 (2005). <https://doi.org/10.1103/PhysRevE.72.011602>
- M. Plapp, *Phys. Rev. E Stat. Nonlin. Soft Matter Phys.* **84**(3), 031601 (2011). <https://doi.org/10.1103/PhysRevE.84.031601>
- G. Boussinot, E.A. Brener, *Phys. Rev. E Stat. Nonlin. Soft Matter Phys.* **89**(6), 060402 (2014). <https://doi.org/10.1103/PhysRevE.89.060402>
- T. Pinomaa, N. Provatas, *Acta Mater.* **168**, 167 (2019). <https://doi.org/10.1016/j.actamat.2019.02.009>
- N.A. Ahmad, A.A. Wheeler, W.J. Boettinger, G.B. McFadden, *Phys. Rev. E* **58**(3), 3436 (1998). <https://doi.org/10.1103/PhysRevE.58.3436>
- D. Danilov, B. Nestler, *Acta Mater.* **54**(18), 4659 (2006). <https://doi.org/10.1016/j.actamat.2006.05.045>
- I. Steinbach, L. Zhang, M. Plapp, *Acta Mater.* **60**(6–7), 2689 (2012). <https://doi.org/10.1016/j.actamat.2012.01.035>
- S. Kavousi, M. Asle Zaeem, *Acta Mater.* **205**, 116562 (2021). <https://doi.org/10.1016/j.actamat.2020.116562>
- A. Mukherjee, J.A. Warren, P.W. Voorhees, *Acta Mater.* **251**, 118897 (2023). <https://doi.org/10.1016/j.actamat.2023.118897>
- W.J. Boettinger, D. Shechtman, R.J. Schaefer, F.S. Biancanello, *Metall. Trans. A* **15**(1), 55 (1984). <https://doi.org/10.1007/BF02644387>
- M. Zimmermann, M. Carrard, M. Gremaud, W. Kurz, *Mater. Sci. Eng. A* **134**(C), 1278 (1991). [https://doi.org/10.1016/0921-5093\(91\)90973-Q](https://doi.org/10.1016/0921-5093(91)90973-Q)
- M. Gremaud, M. Carrard, W. Kurz, *Acta Metall. Mater.* **39**(7), 1431 (1991). [https://doi.org/10.1016/0956-7151\(91\)90228-S](https://doi.org/10.1016/0956-7151(91)90228-S)
- M. Carrard, M. Gremaud, M. Zimmermann, W. Kurz, *Acta Metall. Mater.* **40**(5), 983 (1992). [https://doi.org/10.1016/0956-7151\(92\)90076-Q](https://doi.org/10.1016/0956-7151(92)90076-Q)
- S.C. Gill, W. Kurz, *Acta Metall. Mater.* **41**(12), 3563 (1993). [https://doi.org/10.1016/0956-7151\(93\)90237-M](https://doi.org/10.1016/0956-7151(93)90237-M)
- S.C. Gill, W. Kurz, *Acta Metall. Mater.* **43**(1), 139 (1995). [https://doi.org/10.1016/0956-7151\(95\)90269-4](https://doi.org/10.1016/0956-7151(95)90269-4)
- M. Gremaud, M. Carrard, W. Kurz, *Acta Metall. Mater.* **38**(12), 2587 (1990). [https://doi.org/10.1016/0956-7151\(90\)90271-H](https://doi.org/10.1016/0956-7151(90)90271-H)
- W. Kurz, R. Trivedi, *Metall. Mater. Trans. A* **27**(3), 625 (1996). <https://doi.org/10.1007/BF02648951>
- J.T. McKeown, A.K. Kulovits, C. Liu, K. Zweier, B.W. Reed, T. Lagrange, J.M.K. Wiezorek, G.H. Campbell, *Acta Mater.* **65**, 56 (2014). <https://doi.org/10.1016/j.actamat.2013.11.046>
- J.T. McKeown, K. Zweier, C. Liu, D.R. Coughlin, A.J. Clarke, J.K. Baldwin, J.W. Gibbs, J.D. Roehling, S.D. Imhoff, P.J. Gibbs, D. Tourret, J.M.K. Wiezorek, G.H. Campbell, *JOM* **68**(3), 985 (2016). <https://doi.org/10.1007/S11837-015-1793-X>
- K. Ji, E. Dorari, A.J. Clarke, A. Karma, *Phys. Rev. Lett.* **130**(2), 026203 (2023). <https://doi.org/10.1103/PhysRevLett.130.026203>
- R. Trivedi, W. Kurz, *Acta Metall.* **34**(8), 1663 (1986). [https://doi.org/10.1016/0001-6160\(86\)90112-4](https://doi.org/10.1016/0001-6160(86)90112-4)
- W. Kurz, B. Giovanola, R. Trivedi, *Acta Metall.* **34**(5), 823 (1986)
- J.W. Cahn, *Acta Metall.* **10**(9), 789 (1962). [https://doi.org/10.1016/0001-6160\(62\)90092-5](https://doi.org/10.1016/0001-6160(62)90092-5)
- M.J. Aziz, T. Kaplan, *Acta Metall.* **36**(8), 2335 (1988). [https://doi.org/10.1016/0001-6160\(88\)90333-1](https://doi.org/10.1016/0001-6160(88)90333-1)
- M.J. Aziz, *Metall. Mater. Trans. A* **27**(3), 671 (1996). <https://doi.org/10.1007/BF02648954>
- M. Asta, C. Beckermann, A. Karma, W. Kurz, R. Napolitano, M. Plapp, G. Purdy, M. Rappaz, R. Trivedi, *Acta Mater.* **57**(4), 941 (2009). <https://doi.org/10.1016/j.actamat.2008.10.020>
- M.I. Mendeleev, M.J. Rahman, J.J. Hoyt, M. Asta, *Model. Simul. Mater. Sci. Eng.* **18**(7), 074002 (2010). <https://doi.org/10.1088/0965-0393/18/7/074002>
- M.J. Aziz, W.J. Boettinger, *Acta Metall. Mater.* **42**(2), 527 (1994). [https://doi.org/10.1016/0956-7151\(94\)90507-X](https://doi.org/10.1016/0956-7151(94)90507-X)
- M. Zimmermann, M. Carrard, W. Kurz, *Acta Metall.* **37**(12), 3305 (1989). [https://doi.org/10.1016/0001-6160\(89\)90203-4](https://doi.org/10.1016/0001-6160(89)90203-4)
- S.R. Coriell, R.F. Sekerka, *J. Cryst. Growth* **61**(3), 499 (1983). [https://doi.org/10.1016/0022-0248\(83\)90179-3](https://doi.org/10.1016/0022-0248(83)90179-3)
- A. Karma, A. Sarkissian, *Phys. Rev. E* **47**(1), 513 (1993). <https://doi.org/10.1103/PhysRevE.47.513>
- A. Karma, A. Sarkissian, *Phys. Rev. Lett.* **68**(17), 2616 (1992). <https://doi.org/10.1103/PhysRevLett.68.2616>
- A.A. Wheeler, W.J. Boettinger, G.B. McFadden, *Phys. Rev. A* **45**(10), 7424 (1992). <https://doi.org/10.1103/PhysRevA.45.7424>
- J.S. Langer, "Models of Pattern Formation in First-Order Phase Transitions," in *Directions in Condensed Matter Physics*, ed. by G. Grinstein, G. Mazenko (World Scientific, Philadelphia, 1986), Vol. 1, p. 165. https://doi.org/10.1142/9789814415309_0005
- Y. Yang, H. Humadi, D. Buta, B.B. Laird, D. Sun, J.J. Hoyt, M. Asta, *Phys. Rev. Lett.* **107**(2), 025505 (2011). <https://doi.org/10.1103/PhysRevLett.107.025505>
- T. Haxhimali, A. Karma, F. Gonzales, M. Rappaz, *Nat. Mater.* **5**, 660 (2006). <https://doi.org/10.1038/nmat1693>
- J.A. Dantzig, P. Di Napoli, J. Friedli, M. Rappaz, *Metall. Mater. Trans. A Phys. Metall. Mater. Sci.* **44**(12), 5532 (2013). <https://doi.org/10.1007/S11661-013-1911-8>
- N. Bergeon, D. Tourret, L. Chen, J.M. Debierre, R. Guérin, A. Ramirez, B. Billia, A. Karma, R. Trivedi, *Phys. Rev. Lett.* **110**, 226102 (2013). <https://doi.org/10.1103/PhysRevLett.110.226102>

49. A.J. Clarke, D. Tournet, Y. Song, S.D. Imhoff, P.J. Gibbs, J.W. Gibbs, K. Fezzaa, A. Karma, *Acta Mater.* **129**, 203 (2017). <https://doi.org/10.1016/j.actamat.2017.02.047>
 50. P. Galenko, *Phys. Rev. E* **76**(3), 031606 (2007). <https://doi.org/10.1103/PhysRevE.76.031606>
 51. P.K. Galenko, E.V. Abramova, D. Jou, D.A. Danilov, V.G. Lebedev, D.M. Herlach, *Phys. Rev. E Stat. Nonlin. Soft Matter Phys.* **84**(4), 041143 (2011). <https://doi.org/10.1103/PhysRevE.84.041143>
 52. J.S. Kim, T. LaGrange, B.W. Reed, M.L. Taheri, M.R. Armstrong, W.E. King, N.D. Browning, G.H. Campbell, *Science* **321**(5895), 1472 (2008). <https://doi.org/10.1126/science.1161517>
 53. G.H. Campbell, J.T. McKeown, M.K. Santala, *Appl. Phys. Rev.* **1**, 041101 (2014). <https://doi.org/10.1063/1.4900509>
 54. T. LaGrange, B.W. Reed, D.J. Masiel, *MRS Bull.* **40**(1), 22 (2015). <https://doi.org/10.1557/mrs.2014.282>
 55. J.T. McKeown, A.J. Clarke, J.M. Wiezorek, *MRS Bull.* **45**(11), 916 (2020). <https://doi.org/10.1557/mrs.2020.273>
 56. A. Pineau, G. Guillemot, D. Tournet, A. Karma, C.-A. Gandin, *Acta Mater.* **155**, 286 (2018). <https://doi.org/10.1016/j.actamat.2018.05.032>
 57. R. Fleurisson, O. Senninger, G. Guillemot, C.-A. Gandin, *J. Mater. Sci. Technol.* **124**, 26 (2022). <https://doi.org/10.1016/j.jmst.2022.02.017>
 58. E. Dorari, K. Ji, G. Guillemot, C.-A. Gandin, A. Karma, *Acta Mater.* **223**, 117395 (2022). <https://doi.org/10.1016/j.actamat.2021.117395>
 59. S. Elahi, R. Tavakoli, I. Romero, D. Tournet, *Comput. Mater. Sci.* **216**, 111882 (2023). <https://doi.org/10.1016/j.commatsci.2022.111882> □

Publisher's note

Springer Nature remains neutral with regard to jurisdictional claims in published maps and institutional affiliations.



Joseph T. McKeown leads the Metallurgy and Advanced Microscopy Group at Lawrence Livermore National Laboratory (LLNL). He received a PhD degree in materials science and engineering from the University of California, Berkeley, in 2007. After a postdoctoral fellowship in the Department of Physics at Arizona State University, he joined LLNL to work on *in situ* studies of phase transformations using dynamic transmission electron microscopy (DTEM). His research interests include TEM, alloy design, advanced manufacturing, and process–structure–property–performance relationships in metals and alloys. McKeown can be reached by email at mckeown3@llnl.gov.



Alain Karma joined Northeastern University in 1988, where he is currently a professor of physics and a College of Arts and Sciences Distinguished Professor. He received his PhD degree in physics from the University of California, Santa Barbara, in 1985. He spent three years on a postdoctoral fellowship in physics at the California Institute of Technology. His research interests include phase-field modeling of a wide range of interface dynamical problems in materials science ranging from alloy solidification to crack propagation to dealloying, and nonlinear dynamics of biological systems with focus on cardiac arrhythmias. Karma can be reached by email at a.karma@northeastern.edu.



Kaihua Ji is a postdoctoral researcher in the Computational Materials Science Group within the Materials Science Division at Lawrence Livermore National Laboratory (LLNL). He received his PhD degree in physics from Northeastern University (NEU) in December 2021. He then held a postdoctoral appointment at NEU before joining LLNL. His research focuses on understanding mesoscale phenomena in material and biological systems that are usually out of equilibrium. Ji can be reached by email at ji5@llnl.gov.



Amy J. Clarke is a distinguished scientist in the Sigma Manufacturing Sciences Division at Los Alamos National Laboratory and holds a faculty joint appointment with the Department of Metallurgical and Materials Engineering at the Colorado School of Mines (Mines). Her research focuses on physical metallurgy and making, measuring, and modeling metallic alloys during processing to realize advanced manufacturing. She received her BS degree from Michigan Technological University and her MS and PhD degrees from Mines in metallurgical and materials engineering. Clarke can be reached by email at aclarke@lanl.gov.